3.2 Rossby Adjustment: Weakly Nonlinear Behavior.

The nonlinear terms neglected in Gill's solution can be expected to remain small over a time of $O(a^{-1})$, where $2a$ is the dimensionless amplitude of the initial discontinuity in fluid depth, assumed <<1. We now discuss some new processes that arise after this time period is exceeded. One is the forward of the front that separates the regions of high and low potential vorticity and that initial lies at the position of the barrier. There is also a variety nonlinear processes that act on the forward and backward Kelvin waves that establish the boundary currents. For a<<1 the Kelvin waves become well separated from the potential vorticity front and the evolution of the two features may be treated separately. When a is $O(1)$, nonlinearities arise immediately after the barrier is removed and it become more difficult to treat specific processes in isolation. This topic is taken up in Section 3.3.

(*a*) Motion of the potential vorticity front: contour dynamics.

Since advection of linear potential vorticity $1+\zeta-\eta$ is neglected in linear shallow water theory, $1+\zeta-\eta$ at any (x,y) remains equal to its initial value. The steady flow that emerges as $t\to\infty$, sometimes referred to as the *wave adjusted state,* maintains $1+\zeta-\eta$=1-a upstream of y=0 and $1+\zeta-\eta$=1+a downstream. As a fluid column crosses y=0 its linear potential vorticity jumps from the first to the second of these values. Of course, the original shallow water equations require the full potential vorticity $q=(1+\zeta)/(1+\eta)$ to be advected by the flow. Thus, the lower q of the upstream region would be carried downstream, leading to modification of the wave-adjusted steady state. The fluid at any t would therefore be divided into two bodies A_u and A_d having q=1-a and q=1+a (Figure 3.2.1a). The boundary C separating these two bodies is a *potential vorticity front*, a material contour across which q is discontinuous. C initially lies along y=0 but later becomes convoluted. The potential vorticity distribution at any time is determined by the location of C.

The time required for the wave adjusted state to be established is roughly the time needed for a Kelvin wave to propagate a few deformation radii. In dimensionless terms both the Kelvin wave speed and the deformation radius are unity and therefore this time scale is $O(1)$. However, the resulting fluid velocities are $O(a)$, so that the time required to advect C one deformation radii is $O(a^{-1})$. For a<<1, C evolves very slowly and, in comparison, the wave adjusted state develops instantaneously. This scale separation was exploited by Hermann, Rhines and Johnson (1989) who realized that for $a\to 0$ the wave adjusted steady state can be considered an initial condition for the calculation of C.

In order to compute the evolution of C, let

$$\eta = a[\eta_\infty(x,y)+\tilde{\eta}(x,y,\tau)] \qquad (3.2.1)$$

where $\tau=a^{-1}t$. The first term on the right hand side represents the wave adjusted state

$$\eta_\infty(x,y)=\frac{\sinh(x)}{\cosh(\frac{1}{2}w)}+\mathrm{sgn}(y)\left\{\frac{\cosh(x)}{\cosh(\frac{1}{2}w)}-1+\frac{4}{w}\sum_{n=1}^{\infty}\frac{(-1)^n}{a_n(1+a_n^2)}\cos(a_n x)e^{-(1+a_n^2)^{1/2}|y|}\right\}, \tag{3.2.2}$$

which can be obtained by taking of limit $t\to\infty$ in Gill's linear solution (3.1.25). This steady state consists of boundary layers on the left and right walls for $y\to$-∞ and +∞, and a crossing region about y=0. The velocity field is geostrophically balanced:

$$u_\infty=-\frac{\partial\eta_\infty}{\partial y} \quad \text{and} \quad v_\infty=\frac{\partial\eta_\infty}{\partial x} \tag{3.2.3a,b}$$

The second term is a correction to the wave adjusted state that varies slowly in time and is determined by the requirement of potential vorticity conservation following fluid motion. The full velocity field is the sum of wave-adjusted and transient parts.

$$u=u_\infty+\tilde{u}(x,y,\tau) \quad \text{and} \quad v=v_\infty+\tilde{v}(x,y,\tau) \tag{3.2.4a,b}$$

Substitution of (3.2.1) and (3.2.4) into the shallow water momentum equations (2.20 and 2.21) then shows that, to lowest order, the correction fields are also geostrophically balanced:

$$\tilde{u}=-\frac{\partial\tilde{\eta}}{\partial y} \quad \text{and} \quad \tilde{v}=\frac{\partial\tilde{\eta}}{\partial x} \tag{3.2.5a,b}$$

The side wall boundary condition $u(\pm w/2,y,t)$=0 implies that $\tilde{u}(\pm w/2,y,\tau)=0$ since $u_\infty(\pm w/2,y,\tau)$=0 has already been imposed. Equation (3.2.5a) then requires $\frac{\partial\tilde{\eta}}{\partial y}(\pm w/2,y,\tau)=0$. It is also necessary that the full solution approaches the wave adjusted solution ($\tilde{\eta}\to$0) as $|y|\to\infty$ and therefore

$$\tilde{\eta}(\pm w/2,y,\tau)=0 \tag{3.2.6}$$

Although the transient solution rearranges the velocity field, it does not alter the surface displacement along the sidewalls. The total transport [2tanh($w/2$)] is therefore unaffected by the motion of the potential vorticity front.

In order to calculate the transient solution, one must go beyond the geostrophic approximation and consider higher order balances. First note that the potential vorticity itself can be written in term of the present variables as

$$\frac{1+\zeta}{1+\eta} = \frac{1+a\zeta_\infty + a\tilde{\zeta}}{1+a\eta_\infty + a\tilde{\eta}} = 1 + a[\zeta_\infty - \eta_\infty + \tilde{\zeta} - \tilde{\eta}] + O(a^2)$$

The *O(a)* perturbation potential vorticity can therefore be partitioned into a wave adjusted part $q_\infty = \zeta_\infty - \eta_\infty$ and a transient part $\tilde{q} = \tilde{\zeta} - \tilde{\eta}$. By definition

$$q_\infty = \mathrm{sgn}(y). \qquad (3.2.7)$$

Furthermore, the geostrophic relation for the transient velocities leads to $\tilde{\zeta} = \nabla^2\tilde{\eta}$ and therefore

$$\tilde{q} = \nabla^2\tilde{\eta} - \tilde{\eta}. \qquad (3.2.8)$$

Substitution of the partitioned velocity and potential vorticity into the full shallow water potential vorticity equation and neglect of $O(a^3)$ terms results in

$$\left(\frac{\partial}{\partial\tau} + (u_\infty + \tilde{u})\frac{\partial}{\partial x} + (v_\infty + \tilde{v})\frac{\partial}{\partial y}\right)(q_\infty + \tilde{q}) = 0. \qquad (3.2.9)$$

Thus $q_\infty + \tilde{q}$ $(= \mathrm{sgn}(y) + \tilde{q})$ is advected by the velocity field composed of the sum of the wave adjusted and transient velocities. A fluid column originating from $y<0$ will initially have $q_\infty = -1$ and $\tilde{q} = 0$. Moreover, $\tilde{q}$ will remain zero as long as the column remains in $y<0$. Upon crossing $y=0$, q_∞ jumps to the value +1 and $\tilde{q}$ jumps to the value (-2) required to conserve $q_\infty + \tilde{q}$. Similarly, fluid that originates in $y>0$ and crosses into $y<0$ has $\tilde{q} = +2$. The situation is summarized in Figure 3.2.1b, which shows that $\tilde{q}$ is non-zero only within lobes of fluid that have crossed $y=0$.

The transient solution can be computed using a method known as *contour dynamics* that was developed by Zabusky, et al. (1979) for two dimensional flows and extended for quasigeostrophic flows (the type under consideration) by Pratt and Stern (1986). Hermann et al (1989) applied the method to the problem at hand in a way that differs only slightly from what is now described.

If the location of the contour C is known at a particular time τ_o, then the distribution of $\tilde{q}$ is known and $\tilde{\eta}(x,y,\tau_o)$ can be found by solving

$$\nabla^2\tilde{\eta} - \tilde{\eta} = \tilde{q}(x,y,\tau_o). \qquad (3.2.10)$$

subject to the boundary conditions (3.2.6). Note that $\tilde{q}(x,y,\tau_o)$ will be non-zero only within a lobed region R (Figure 3.2.1b). The solution can be expressed in terms of the Green's function $G(x,y;\xi,\mu)$ defined by

$$\nabla^2 G - G = \delta(\xi)\delta(\mu) \quad \text{and} \quad G=0 \text{ at } (x=\pm w/2). \qquad (3.2.11).$$

Thus

$$\tilde{\eta}(x,y,\tau_o) = \iint_R \tilde{q}(x,y,\tau_o) G(x,y;\xi,\mu) d\mu d\xi . \qquad (3.2.12)$$

The velocity fields $(\tilde{u},\tilde{v})$ can be found by differentiating this $\tilde{\eta}$ and adding the results to the known (u_∞,v_∞). As discussed below, $(\tilde{u},\tilde{v})$ can be expressed in terms of a contour integral around the edge ∂R of region *R*. Since the contour *C* is advected by this total velocity, the position of *C* at $\tau_o+\Delta\tau$ can be estimated. Then (3.2.12) can be applied to the new $\tilde{q}$ to determine the corresponding surface elevations and velocities. These steps are then repeated leading to an iterative procedure that can be implemented numerically. Note that the solution will remain independent of *a*, which has dropped out of the analysis. The channel width *w* is now the only remaining parameter.

A convenient and computationally efficient form of the Green's function is

$$G(x,y;\xi,\mu) = \frac{1}{2\pi}\sum_{n=-\infty}^{\infty}(\mathrm{K}_{1,n} + \mathrm{K}_{2,n}), \qquad (3.2.13)$$

where

$$\mathrm{K}_{1,n} = -K_o\left\{\left[(x-\xi-2nw)^2 + (y-\mu)^2\right]^{1/2}\right\},$$

$$\mathrm{K}_{2n} = K_o\left\{\left[(x+\xi+w+2nw)^2 + (y-\mu)^2\right]^{1/2}\right\},$$

and K_o denotes the modified Bessel function of zero order.

In advance of the actual computation, a certain amount of physical intuition can be gained by careful consideration of (3.2.13). First consider the term $\mathrm{K}_{1,0}$:

$$\mathrm{K}_{1,0} = -K_o\left\{\left[(x-\xi)^2 + (y-\mu)^2\right]^{1/2}\right\}$$

describing a cyclonic point vortex centered at $(x,y)=(\xi,\mu)$. At large distances from the center, the free surface displacement and associated cyclonic swirl velocity decay exponentially. The decay scale is the Rossby Radius of deformation, here unity. In an infinite domain, this term would comprise the entire Green's function. An isolated eddy composed of a patch of uniform potential anomaly $\tilde{q} = \tilde{q}_o$ would have an η field obtained by integrating $\tilde{q}_o$ times this Green's function over the area of the patch.

If a single boundary in the form of a wall at $y=w/2$ is present, the boundary condition can be satisfied by adding an image vortex to a hypothetical body of fluid lying inside the wall (Figure 3.2.2a). The image vortex is equal in strength but opposite in sign and is located an equal distance inside the wall. The *x*-velocity at the wall created by the image is equal and opposite to that due to the original vortex. The condition of zero normal flow is thereby satisfied. Note that the image for $\mathrm{K}_{1,0}$ is $\mathrm{K}_{2,-1}$ and that the velocity

field created by the latter causes the original vortex to move parallel to the wall. An anticyclonic vortex will move towards negative *y* whereas a cyclonic vortex will move towards positive *y*. The motion is identical to that of a dipole (a pair of equal and opposite vorticies).

The boundary condition problem for the normal velocity become more difficult in the presence of two walls (Figure 3.2.2b). Beginning with the images $K_{1,0}$ and $K_{2,-1}$ one could add a third $K_{2,0}$ beyond the wall at $x=-w/2$. Alone, $K_{1,0}$ and $K_{2,0}$ would satisfy the boundary condition at $x=-w/2$. The original image vortex $K_{2,-1}$ gives rise to a small non-zero u at $x=-w/2$ but this vortex since lies further from $x=-w/2$ than either $K_{1,0}$ or $K_{2,0}$. Since the velocity field of $K_{2,-1}$ decays away exponentially there is hope that the error in the boundary condition at $x=-w/2$ might not be too large. The same remarks can be made for the pair $K_{1,0}$ and $K_{2,-1}$ which alone would satisfy the boundary condition at $x=w/2$ if not for the presence of $K_{2,0}$.

In order to construct a Green's function that exactly satisfies the condition $u=0$ on both walls, it is necessary to add further images at successively larger distances from the walls. For example , the contaminating effect of the $K_{2,-1}$ on the boundary condition at $x=-w/2$ can be countered by adding its image $K_{1,1}$ (Figure 3.2.2c). The contaminating effect of the $K_{2,0}$ on the boundary condition at x=w/2 can be countered by adding its image $K_{1,1}$. In general, $K_{1,n}$ corrects $K_{2,n-1}$ for ($n\geq 0$) whereas $K_{1,n}$ corrects $K_{2,n}$ for ($n<0$). The series in (3.2.13) is constructed following this principle. As the reader might gather from an inspection of Figure 3.2.2c the effect of adding all the extra images is to somewhat retard the dipole effect mentioned earlier. Thus the primary vortex $K_{1,0}$ does not move towards larger values of *y* as rapidly. In fact, a single vortex placed at the centerline $x=0$ of the channel would not translate at all.

The geostrophic velocities for the transient solution can be obtained from (3.2.12) as

$$\nabla_{(x,y)}\tilde{\eta}(x,y,\tau_o) = (\tilde{v},-\tilde{u}) = \iint_R \nabla[\tilde{q}(x,y,\tau_o)G(x,y;\xi,\mu)]d\xi d\mu \qquad (3.2.14)$$

where $\nabla_{(x,y)} = \frac{\partial}{\partial x} + \frac{\partial}{\partial y}$. The region R of anomalous potential vorticity is composed of several sub-regions or lobes, each of which contain fluid of uniform $\tilde{q}$. Consider a sub-region R_o for which $\tilde{q} = \tilde{q}_o$ (Figure 3.2.3a). The contribution to the integral in (3.2.14) from this sub-region is

$$
\begin{aligned}
I_{R_o} &= \tilde{q}_o \iint_{R_o} \nabla_{(x,y)} G(x,y;\xi,\mu) d\mu d\xi \\
&= \frac{\tilde{q}_o}{2\pi} \iint_{R_o} \sum_{n=-\infty}^{\infty} (\nabla_{(x,y)} \mathrm{K}_{1,n} + \nabla_{(x,y)} \mathrm{K}_{2,n}) d\mu d\xi \\
&= -\frac{\tilde{q}_o}{2\pi} \iint_{R_o} \sum_{n=-\infty}^{\infty} (\nabla_{(\xi,\mu)} \mathrm{K}_{1,n} + \nabla_{(-\xi,\mu)} \mathrm{K}_{2,n}) d\mu d\xi \\
&= -\frac{\tilde{q}_o}{2\pi} \oint_{\partial R_o} \sum_{n=-\infty}^{\infty} \left[\mathrm{K}_{1,n}(d\bar{\mu}, d\bar{\xi}) + \mathrm{K}_{2,n}(-d\bar{\mu}, d\bar{\xi}) \right]
\end{aligned}
\qquad (3.2.15)
$$

The third step is made possible by the $(x \leftrightarrow -\xi, y \leftrightarrow -\mu)$ symmetry in $\mathrm{K}_{1,n}$ and by the $(x \leftrightarrow \xi, y \leftrightarrow -\mu)$ symmetry in $\mathrm{K}_{2,n}$. The final step follows from application of Green's theorem. The contour integral is performed counterclockwise around the edge ∂R_o of R_o.

In the problem at hand, where $\tilde{q}_o$ equals +2 or -2, depending on the sub-region, application of (3.2.15) over each sub-region and summation of the results leads to

$$
(\tilde{v}, -\tilde{u}) = \frac{1}{\pi} \oint_{\partial R} [\sum_{n=-\infty}^{\infty} [K_{1,n}(d\bar{\mu}, d\bar{\xi}) + K_{2,n}(-d\bar{\mu}, d\bar{\xi})]] \qquad (3.2.16)
$$

where the integration circuit ∂R is shown in Figure 3.2.3b and the direction of integration is such as to keep higher $\tilde{q}$ values on the right. In normal practice the evolution of ∂R is calculated by seeding a group of material points along it and using (3.2.16) to follow the motion of each point. If $(x_n(t), y_n(t))$ represents the coordinates of point n, then

$$
dx_n / dt = u(x_n, y_n) \quad \text{and} \quad dy_n / dt = v(x_n, y_n) ,
$$

with u and v given by (3.2.16). These relations are integrated numerically over a small time increment for all the material points on ∂R and the new positions are used to update ∂R. In this way, the evolution of the potential vorticity front can be calculated without having to explicitly consider any quantities measured away from the front.

Examples of the solutions reveal significant departures from the linear case, even when the channel is very wide (Figures 3.7 and 3.8). On the right-hand side of the channel, the front is carried rapidly downstream by the boundary layer flow and its leading edge has moved beyond the Figure 3.2.4 frame boundary by τ=10. More significantly, there is a tendency for the front to move towards positive y along the *left* wall. In the channel interior the front roughly maintains its original position. [The apparent movement of the interior front towards negative y is actually due to the fact that the plot is made in a frame of reference moving with the mean velocity $U=2w^{-1}\tanh(w/2)$.]

The intrusion of low potential vorticity fluid along the left wall is due primarily to the image effect described above. The lobe of intruding fluid that is bounded by the potential vorticity front on the right, the wall x=-w/2 on the left, and y=0 has potential vorticity anomaly $\tilde{q}$=-2 as suggested in Figure 3.2.4. The vorticity of this blob is therefore anticyclonic, as can be verified by performing the integration in (3.2.12) and calculating the corresponding geostrophic velocities. (There is a contribution to this integral from the lobe of fluid intruding along the right wall as well, but this lobe is quite far away and its range of influence does not extend to the left wall.) In order to satisfy the left wall boundary condition u=0, the anticyclonic lobe must have a cyclonic image lobe and the tendency of the latter is to advect the anticyclonic fluid towards positive y.

Associated with the left-wall intrusion is an overshooting across y=0 of the boundary current along the same wall (Figure 3.2.5). Further downstream the boundary current veers away from wall and reverses course. The current returns to y=0 where it crosses the channel. As time progresses the intrusion widens and the crossing rout increasingly departs from y=0. Hermann et al (1989) speculate that eventually the crossing route will be swept downstream and that the final steady state at *any* fixed y will eventually become one with only a left-wall boundary layer. Confirmation is made for the case the case $w=10$, where the downstream movement of the potential vorticity front is clear (Figure 3.2.6a). As the front moves away from the original position of the barrier, the cross-sectional profile of surface elevation there evolves to the point where only a left-wall boundary flow remains (Figure 3.2.6b).

The loss at y=0 of the cross flow presents difficulties for the principle of geostrophic control. If we choose points A and B (Figure 3.2.3) as our interior reference locations, then the total transport 2tanh($w/2$) is initially bounded by the value $\eta_A - \eta_B = 2$, as required. After the potential vorticity front travels beyond B, however, η_A and η_B become equal and the bound fails. Thus, geostrophic control applies after the wave-adjusted flow is established but before the potential vorticity dynamics have affected the final adjustment.

The foregoing results suggest that geostrophic control might apply in systems where the time dependence is imposed by the tides or some other oscillatory forcing. The forcing period T must be longer than the wave adjustment time in order to allow the cross-channel flow to become established. The wave adjustment time is roughly, the deformation radius $(gD)^{1/2} / f$ divided by the Kelvin wave speed $(gD)^{1/2}$. In addition T must be much shorter than the advective time of the potential vorticity front, else the crossing flow will be carried away. The advective time is at least (D/a^*) times the wave adjustment time, where a^* is now the (dimensional) tidal amplitude. Thus the principle of geostrophic control appears then to require

$$1 << Tf << \frac{D}{a^*} \ . \qquad (3.2.17)$$

(Pratt, 1991). As shown by the calculations of Herman et al. (1989) the upper bound in (3.2.17) may be overly conservative when the channel is much wider than the deformation radius.

Middleton and Viera (1991) and Hannah (1992) have assessed the validity of the geostrophic control in the Bass Strait, the channel separating Tasmania from Australia. When a low frequency (240 hr) wind and pressure forcing period is used for T, (3.2.17) is satisfied and geostrophic control holds, at least in their models. If one or both of the neighboring basins is effectively finite in extent, which is apparently not a problem for the Bass Strait, then the above arguments become complicated. A Kelvin wave can circle the basin and return to the strait. Wright (1987) has investigated models of this behavior and found that geostrophic control typically does not hold.

(b) Kelvin/Poincaré wave interactions.

Given sufficient time, weak nonlinearities can also alter the character of the transients that set up the wave-adjusted state. A numerical solution[1] obtained by Tomasson and Melville (1992) for a=.15 and w=2 (Figure 3.2.7a) gives an overview. The solution is obtained by integrating the Boussinesq equations, an approximation to the full Euler equations permitting weak nonlinearity and weak nonhydrostatic effects. One of the most striking differences with Gill's linear solution is the lack of symmetry between the forward and backward moving waves. The forward waves, especially the region $75<y<210$, contains an abundance of smaller spatial scales, while the backward moving waves ($-200<y<75$) remain relatively smooth. Another difference is that the leading edges of the wave (near $y=\pm 210$) exhibit curvature. An enlarged view of the forward waves (Figure 3.2.7b) shows this feature clearly. The leading edge of the advancing front is perpendicular to the right wall at the wall, but becomes increasingly oblique as one moves away from this wall. This aspect will be addressed further in Section 3.6.

A physical process that accounts for much of the new behavior is the resonant excitation of Poincaré waves by finite amplitude Kelvin waves. According to the linear solution, the removal of the barrier at y=0 excites two Kelvin waves that move away along their respective walls. Poincaré waves are also generated but they are outrun by the Kelvin waves, which have larger group speeds. There is a tendency for the forward-propagating Kelvin wave to steepen and the backward-propagating Kelvin wave to rarefy, as described in Section 2.2. The smaller the step size a, the more slowly the steepening or rarefacation occurs. For sufficiently large a, the forward Kelvin wave may break, leading the formation of a shock. This process is discussed in the next few sections. However, for moderate or small values of a, the steepening process may be arrested by dispersive effects due to nonhydrostatic accelerations. The equilibrated, finite-amplitude Kelvin wave propagates a bit more rapidly than its linear counterpart.

[1] To obtain this solution, the initial step in depth was slightly smoothed, so there is no distinct potential vorticity front.

Now consider the linear dispersion relations Poincaré and Kelvin waves in a channel geometry(Figure 3.2.8 and equations 2.1.28 and 2.1.29). The forward Kelvin wave has frequency $\omega^* = (gD)^{1/2} l^*$, as represented by the straight line. The effect of the nonlinear increase of speed for the forward Kelvin wave can qualitatively be demonstrated by increasing the slope of this line. Doing so causes this (dashed) line to intersect the dispersions curves for the Poincaré modes. A slight increase in slope leads to intersections only at high wave numbers. At the intersection points the phase speed of a Poincaré mode matches that of the Kelvin mode, a necessary condition for nonlinear interaction between the two. The Poincaré modes feed on energy contained in the Kelvin wave. Their presence accounts for some of the wave activity behind the leading edge of the forwards Kelvin wave. The energy drain causes the Kelvin wave amplitude to gradually decay and the process of energy transfer is gradually attenuated. Since the backwards Kelvin wave rarefies, the slope of the corresponding dispersion curve $\omega^* = -(gD)^{1/2} l^*$ decreases, moving it away from those of the Poincaré modes. Thus the region to the rear of the backward advancing wave front is relatively free of wave activity.

Random Notes and Questions

Should I show T&M Figure 15b, which shows peaks in the spectra of the first five Poincare modes near the resonant values of k, as predicted from the measured speed of the nonlinear leading Kelvin wave? The peaks do not lie right at the expected resonances, and some modes display double peaks. M&T suggest the difference may be due to the strong forcing or the appearance of more than one nonlinear Kelvin wave.

Questions: Is it only the nonhydrostatic dispersion that halts the steepening? We know that non-semigeostrophic effects can do the same. Which is most important in Tomasson and Melville's case?
Can you get the same type of effects with a nonhydrostatic model?

Is there a fairly simple way of presenting a weakly nonlinear theory?
Grimshaw 1985 and Katsis and Akylas 1987 have written about a theory that results in the KP equation) and Melville, Tomasson and Renouard (1989)talk about a coupled evolution equation (CEE). Another reference to the KP eq. is Grimshaw and Melville 1989 in Stud. Appl. Maths (in press as of 1989). Unfortunately, the later was developed by Macomb 1986 in a MIT M.S. thesis (Dept. of Civil Engineering, 1986) and I have not found a derivation anywhere. In his 1989 paper with Tommason and Renouard, Melville states that "all but the final steps of the derivation of the CEE are identical to the derivation of the rotation-modified KP equation, which is derived in detail by Grimshaw and Melville 1989 in Stud. Appl. Maths (in press as of 1989). This is all discussed p. 3 and 4 of Melville, et al JFM 89. Then there is the present analysis based on the Boussinesq equations, which are quite easy to derive.

PHOTOS and OBSERVATIONS

There are a number of photos showing the curvature of the Kelvin wave front that might look good in the book. For example

Maxworthy '83, JFM 129 did some experiments with an intrusion between upper and lower fluids. A bit hard for me to separate the intrusion dynamics from the Kelvin wave dynamics. For example, there is some KH instability around the edge of the intrusion. But emphasizes the curvature of the Kelvin wave front (and trailing Kelvin waves-all considered solitons). Photos show the intrusion but I can't see the waves crests and troughs. However there is a drawing (Fig. 11) made from observations of waves in Knight Inlet, the shape of an internal wave propagating through the strait and showing curvature. The drawing was made from a photo of Farmers. Also, Figure 12 shows a satellite image of the 'Buster' showing backward curvature. Hard to see what this is. Taken from a reference of Baines.

Renouard et al JFM177, '87 and a Figure 7 showing shadow plots of curving wave crests with an accompanying drawing.

All of these references are in my chapter 3 folder.

Exercises

1) Find the wave adjusted steady state $\eta_\infty(x,y)$ using local conservation of linearized potential vorticity. That is, use the same approach as in the Rossby adjustment problem on an infinite plane, as discussed at the beginning of Section 3.1. First show that the mathematical problem is

$$\nabla^2\eta_\infty - \eta_\infty = \mathrm{sgn}\, y$$

subject to the boundary conditions

$$\eta_\infty = \pm\tfrac{1}{2}\tanh(\tfrac{1}{2}w) \qquad (x = \pm\tfrac{1}{2}w)$$

and

$$\eta_\infty \to \pm\left[-1 + \frac{e^{\pm x}}{\cosh(\frac{1}{2}w)}\right] \qquad (y \to \pm\infty)$$

(Note: these boundary conditions are deduced from the solution for K in the Kelvin wave part of the solution.) Then solve for the wave adjusted state.

2) *Propagation tendency of a potential vorticity wedge*. As a crude model of the behavior near the leading edge of the left-wall intrusion, consider a semi-infinite wedge of fluid with $\tilde{q}$=-2 intruding into a ambient fluid with $\tilde{q}$=0. As shown in Figure 3.2.7 the outside edge of the wedge forms an angle θ with the wall. Show that the velocity v=v_L at the leading edge of the wedge is given by:

$$v_L = 1 - \cos(\theta). \qquad (3.2.17)$$

(The identity $\int_0^\infty K_o(y)dy = \frac{\pi}{2}$ may prove helpful.)

By consideration of the image of the wedge, deduce the nose speed for a wedge of potential vorticity $\tilde{q} = 2$ propagating along a right wall:

$$v_R = \cos(\theta) - 1. \qquad (3.2.18)$$

For $\theta<\pi/2$, $v_L>0$ while $v_R<0$. In the Rossby channel problem, however, a background velocity v_∞ exists along the right wall and this tends to advect the wedge towards positive y. The net result is that the wedge moves towards positive y at something less than the advective speed.

By a more complicated analysis (Hermann et al 1989) it is also possible to demonstrate that the left wall wedge will steepen and the right wall wedge will rarify, as observed in the numerical solutions for large values of w.

Hint: use equation 3.2.16

Figure Captions

3.2.1 Definition sketches showing potential vorticity front (a) and potential vorticity anomalies (b).

3.2.2 Point vorticies and images needed to satisfy the condition of no normal flow at the channel sidewalls.

3.2.3 (a): Integration contour about the lobe R_o of anomalously low potential vorticity. (b): Integration contour for the entire region of anomalous potential vorticity.

3.2.4 Evolution of the potential vorticity front for the case w=25. In order to visually separate the contour at different times, the results are plotted in a frame of reference x' that translates towards positive x at speed .08. The original position of the barrier (x=0) at τ=20 is indicated by a dashed line. (Based on Figure 4 or Hermann et al. 1989)

3.2.5 Evolution of the surface elevation (η) field for the case shown in Fig. 3.2.4. (Based on Figure 8 of Hermann et al. 1989)

3.2.6 (a) The evolution of the potential vorticity front for the case w=10. The portions of the curves near the side walls have been carried downstream and out of the frame. (b) The corresponding surface elevation (η) field. (Figure 9 of Hermann et al. 1989)

3.2.7 Surface elevation (η) field at t=200 based on a numerical solution to the dam break problem. Frame (b) shows the region near the edge of the forward wave front. (Tomasson and Melville, 1992, Figure 12.)

3.2.8 Dispersion relations for Poincaré and Kelvin waves. The dimensional frequency and along-channel wave number are denoted by ω^* and l^*.

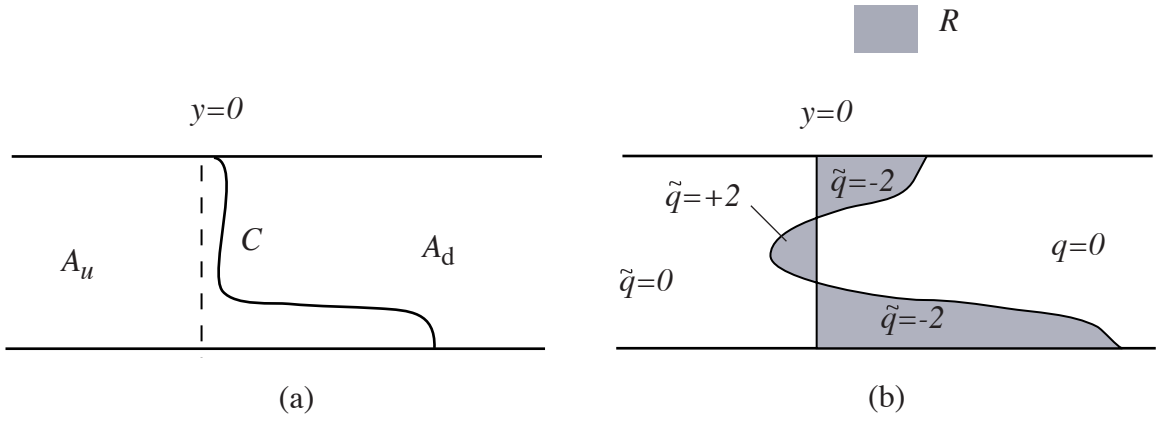

Figure 3.2.1

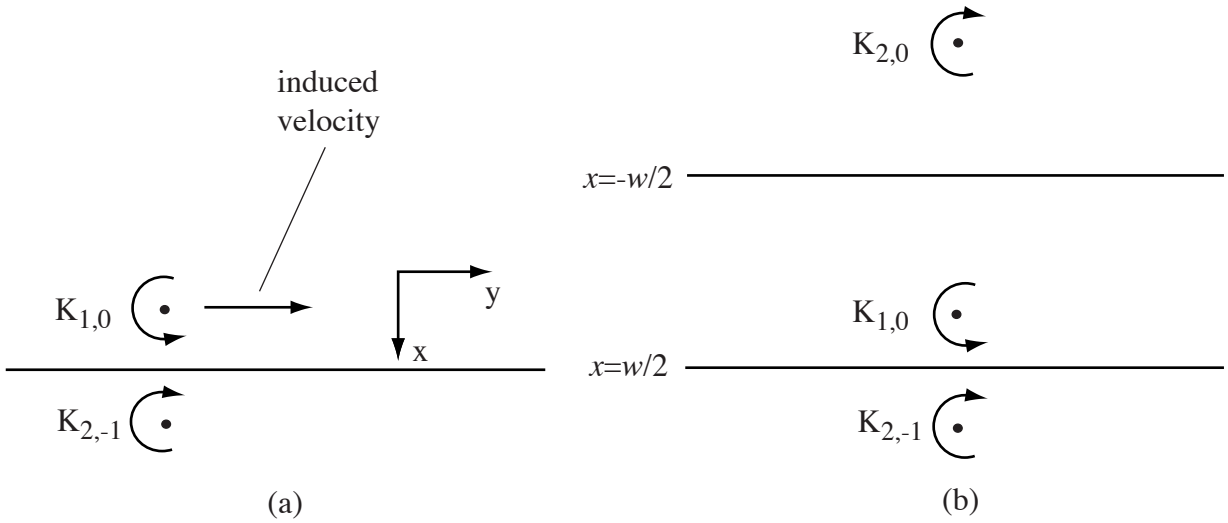
induced
velocity
$K_{1,0}$
$K_{2,-1}$
y
x
(a)
$K_{2,0}$
x=-w/2
$K_{1,0}$
x=w/2
$K_{2,-1}$
(b)

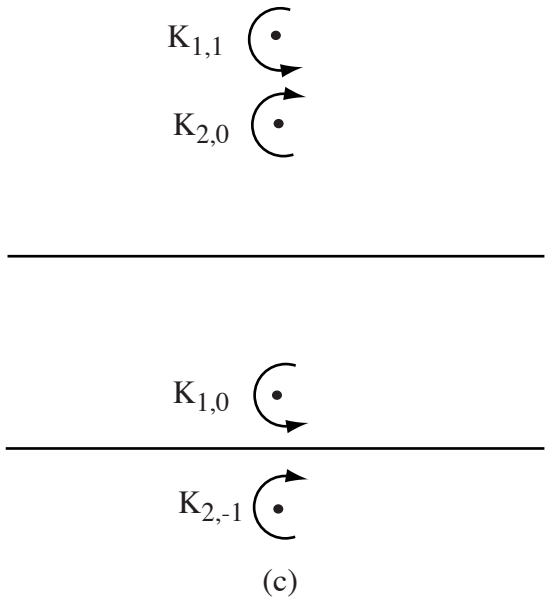
$K_{1,1}$
$K_{2,0}$
$K_{1,0}$
$K_{2,-1}$
(c)

Figure 3.2.2

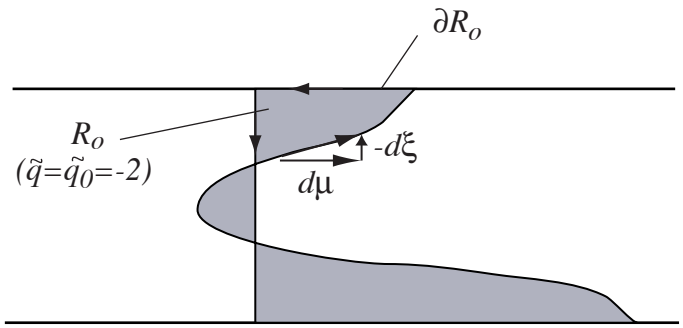

(a)

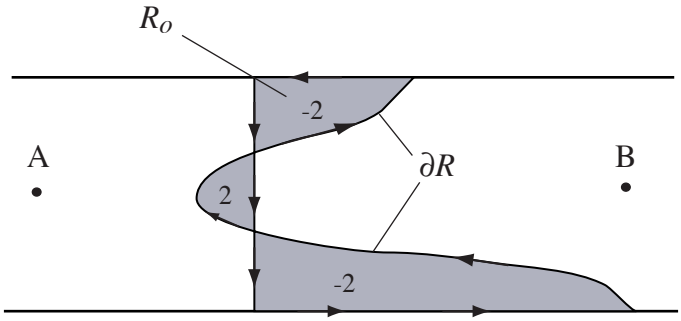

(b)

Figure 3.2.3

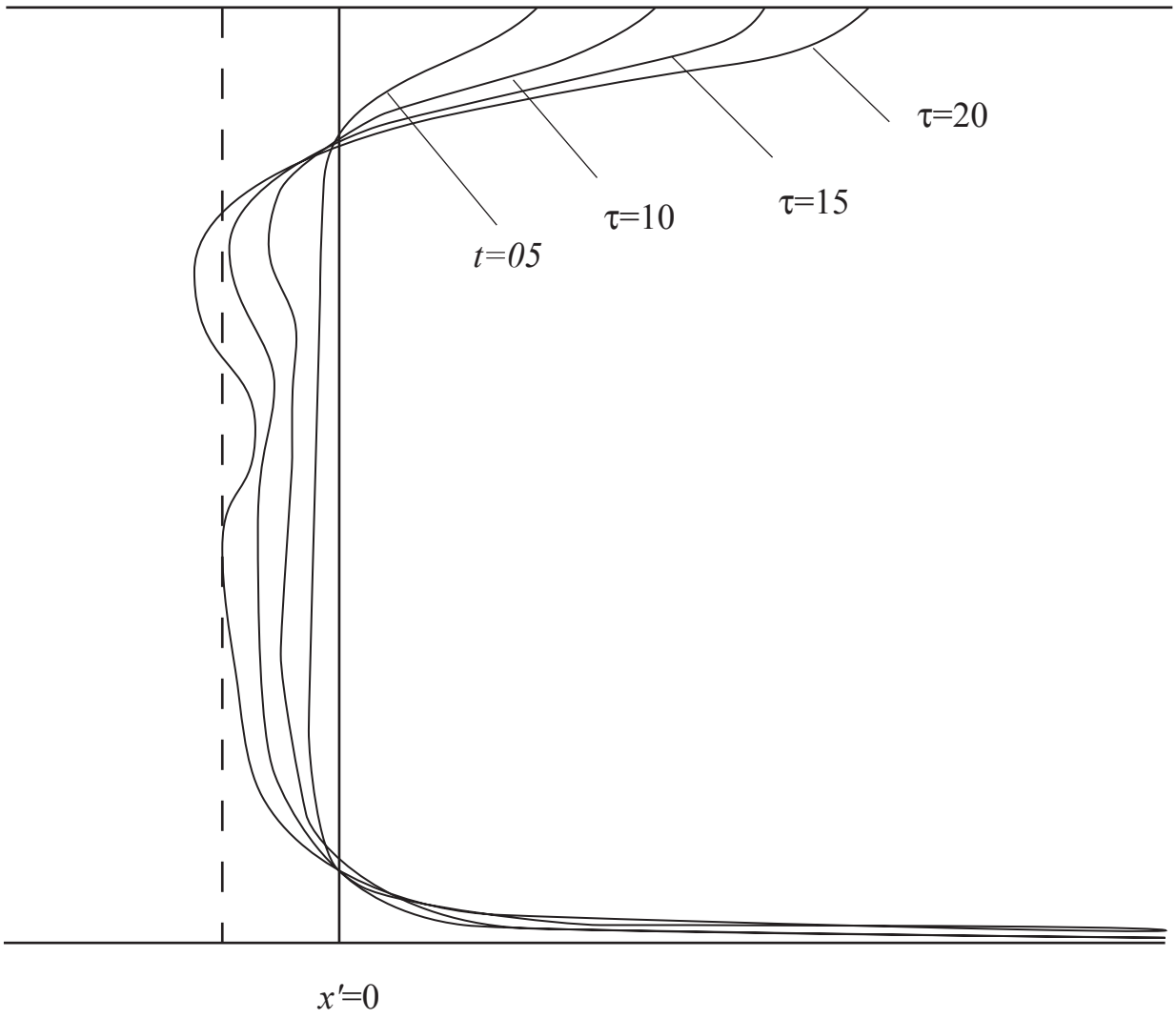

Figure 3.2.4

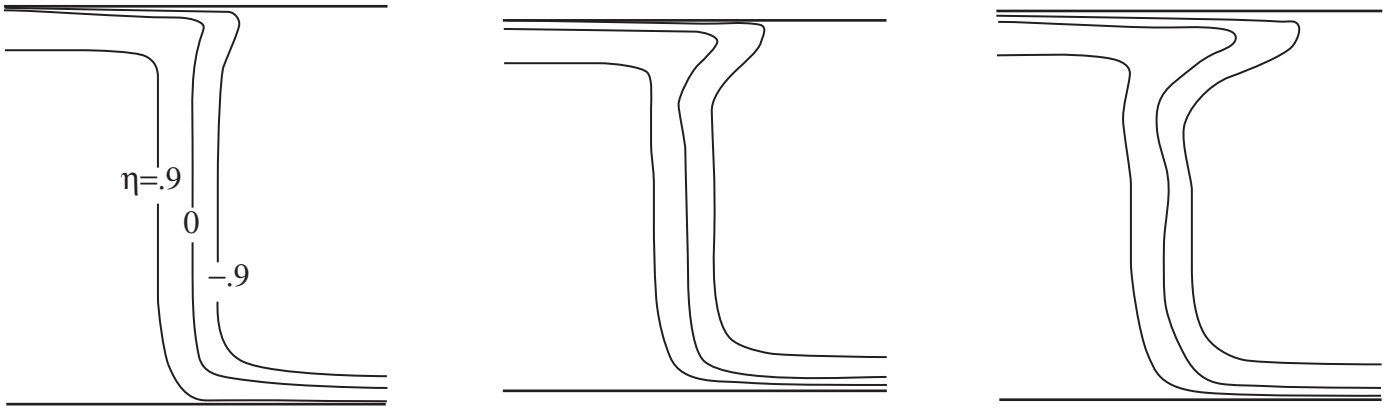

Figure 3.2.5

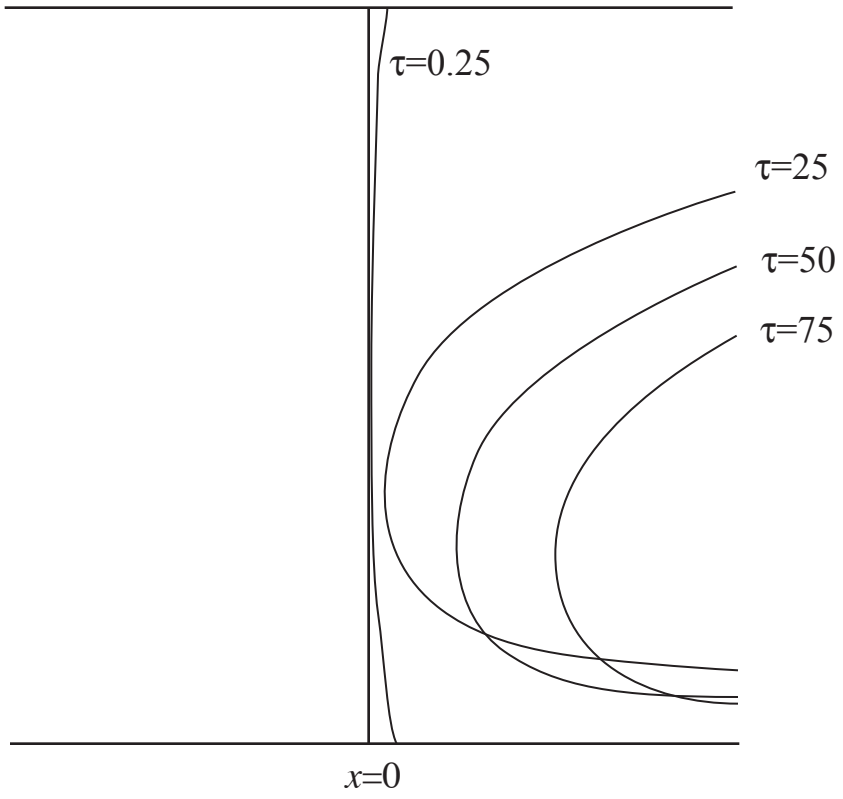

Figure 3.2.6a

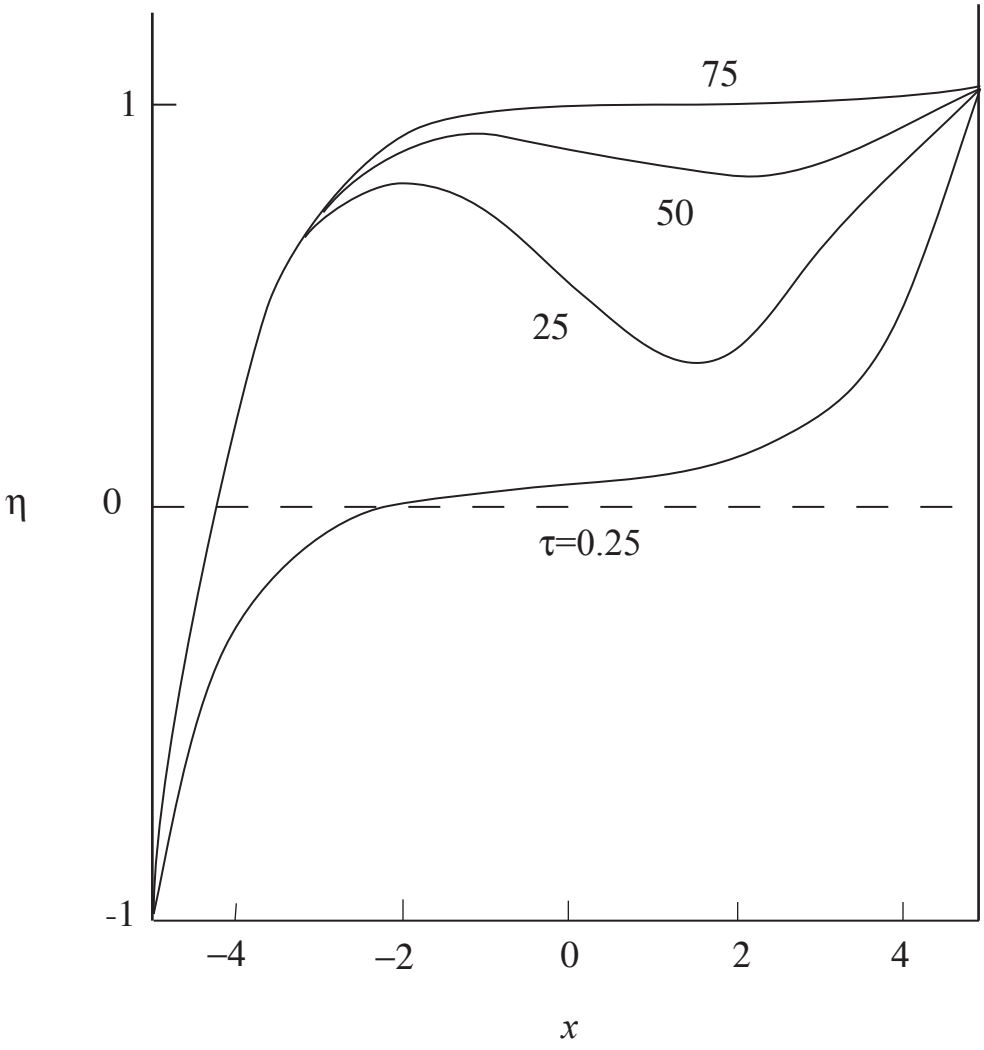

Figure 3.2.6b

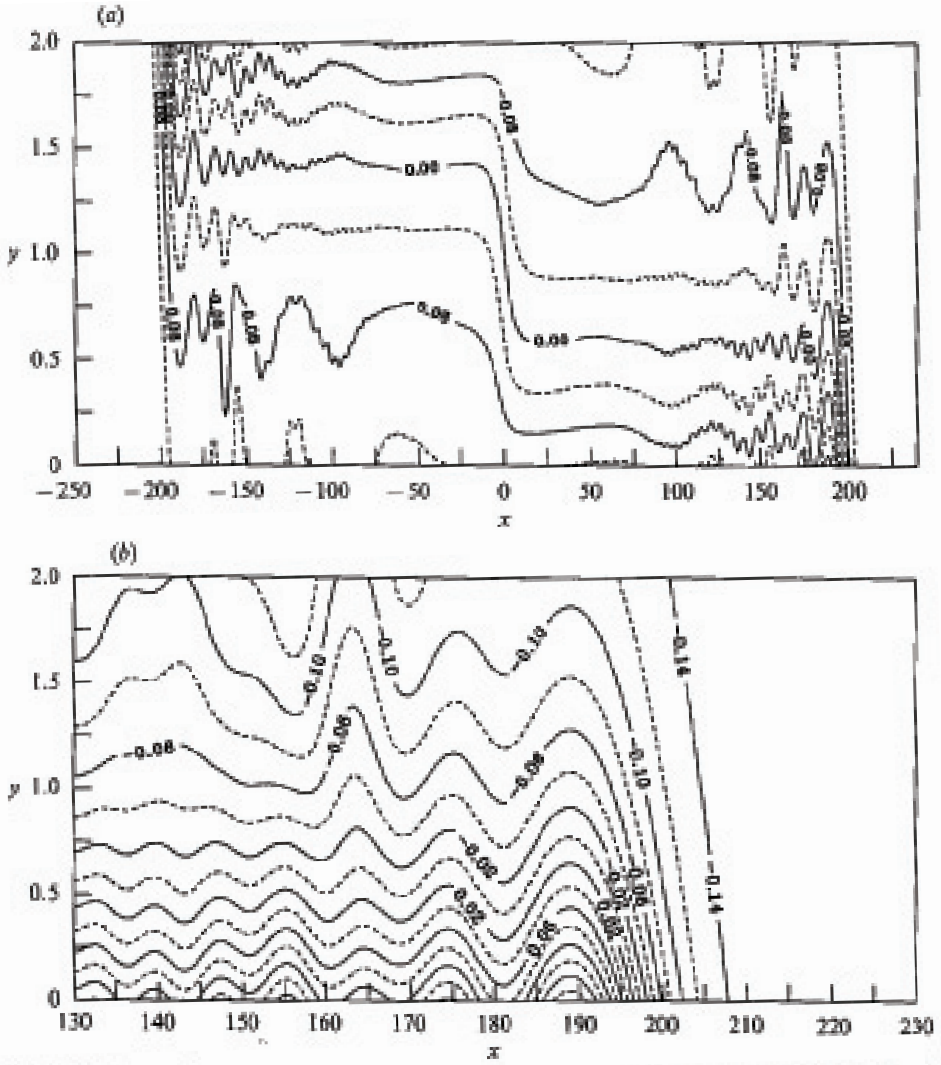

FIGURE 10. Contour plots of the solution of linearized versions of (3.1)–(3.3) for η at $t = 200$ for the step of semi-infinite length. (a) The solution over the whole channel. (b) The leading disturbance moving to the right.

Figure 3.2.7 (scan)

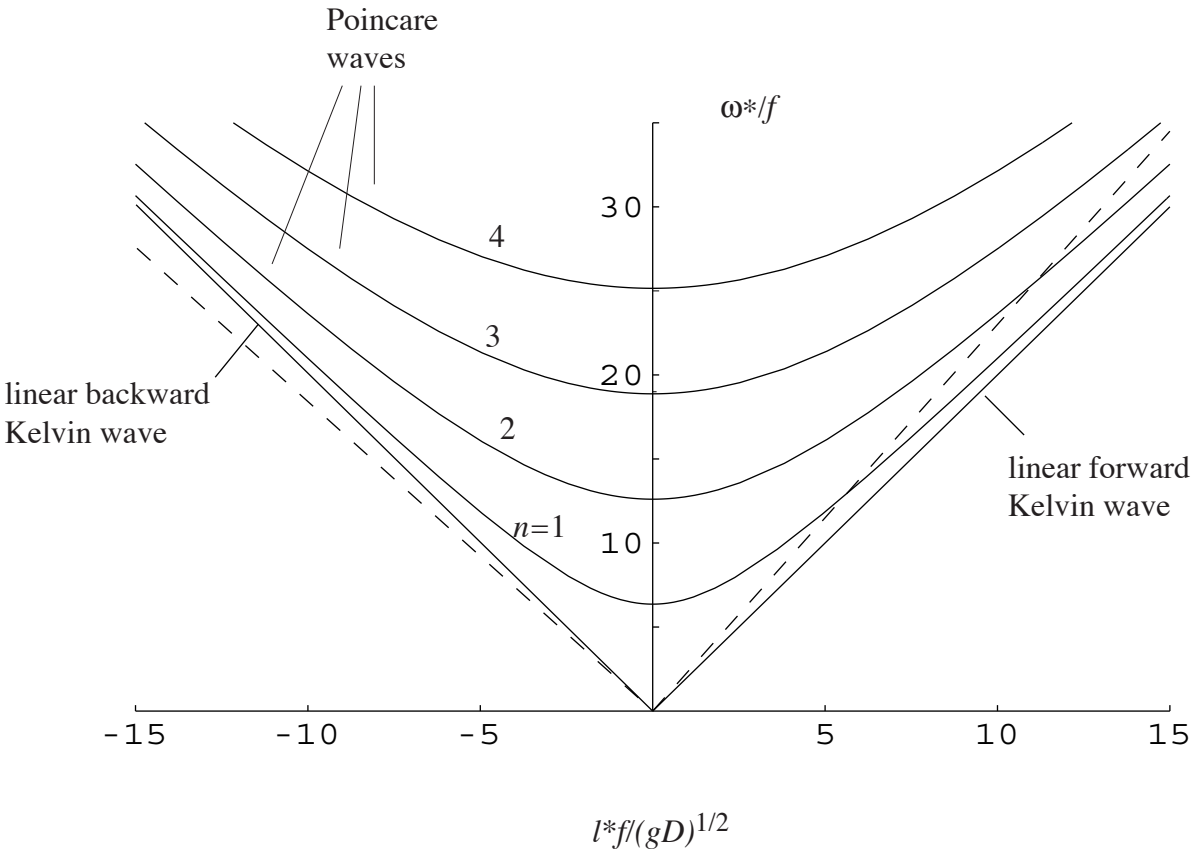
Poincare
waves
ω*/f
30
20
10
4
3
2
n=1
linear backward
Kelvin wave
linear forward
Kelvin wave
-15
-10
-5
5
10
15
l*f/(gD)^1/2

Figure 3.2.8